RESEARCH ARTICLE | MARCH 15 2024

Mapping orthorhombic domains with geometrical phase analysis in rare-earth nickelate heterostructures

Bernat Mundet ; Marios Hadjimichael ; Jennifer Fowlie ; Lukas Korosec ; Lucia Varbaro ; Claribel Domínguez; Jean-Marc Triscone ; Duncan T. L. Alexander

APL Mater. 12, 031124 (2024)
https://doi.org/10.1063/5.0180998

APL Materials ARTICLE pubs.aip.org/aip/apm

Mapping orthorhombic domains with geometrical phase analysis in rare-earth nickelate heterostructures

Cite as: APL Mater. 12, 031124 (2024); doi: 10.1063/5.0180998
Submitted: 13 October 2023 • Accepted: 8 February 2024 •
Published Online: 15 March 2024

View Online Export Citation CrossMark

Bernat Mundet,[1,2,a)] Marios Hadjimichael,[1,b)] Jennifer Fowlie,[1,c)] Lukas Korosec,[1] Lucia Varbaro,[1] Claribel Domínguez,[1] Jean-Marc Triscone,[1] and Duncan T. L. Alexander[2]

AFFILIATIONS

[1] Department of Quantum Matter Physics, University of Geneva, Geneva, Switzerland
[2] Electron Spectrometry and Microscopy Laboratory (LSME), Institute of Physics (IPHYS), École Polytechnique Fédérale de Lausanne (EPFL), Lausanne, Switzerland

[a)] **Author to whom correspondence should be addressed:** bernat.mundet@icn2.cat. **Present address:** Catalan Institute of Nanoscience and Nanotechnology (ICN2), Bellaterra, Spain.
[b)] **Present address:** Department of Physics, University of Warwick, Coventry, United Kingdom.
[c)] **Present address:** Stanford University, Stanford, California 94305, USA.

ABSTRACT

Most perovskite oxides belong to the *Pbnm* space group, composed of an anisotropic unit cell, *A*-site antipolar displacements, and oxygen octahedral tilts. Mapping the orientation of the orthorhombic unit cell in epitaxial heterostructures that consist of at least one *Pbnm* compound is often needed for understanding and controlling the different degrees of coupling established at their coherent interfaces and, therefore, their resulting physical properties. However, retrieving this information from the strain maps generated with high-resolution scanning transmission electron microscopy can be challenging, because the three pseudocubic lattice parameters are very similar in these systems. Here, we present a novel methodology for mapping the crystallographic orientation in *Pbnm* systems. It makes use of the geometrical phase analysis algorithm, as applied to aberration-corrected scanning transition electron microscopy images, but in an unconventional way. The method is fast and robust, giving real-space maps of the lattice orientations in *Pbnm* systems, from both cross section and plan-view geometries, and across large fields of view. As an example, we apply our methodology to rare-earth nickelate heterostructures, in order to investigate how the crystallographic orientation of these films depends on various structural constraints that are imposed by the underlying single crystal substrates. We observe that the resulting domain distributions and associated defect landscapes mainly depend on a competition between the epitaxial compressive/tensile and shear strains, together with the matching of atomic displacements at the substrate/film interface. The results point toward strategies for controlling these characteristics by appropriate substrate choice.

I. INTRODUCTION

Transition metal perovskite oxides, with the chemical formula ABO_3, consist of a pseudocubic structure composed of a central *B*-site transition metal cation octahedrally coordinated with six oxygen atoms (face-centered positions) and eight *A*-site cations situated at the corner-sharing positions. In the ideal cubic structure, the *B*–O–*B* bond angle between the transition metal and the neighboring oxygen atoms is 180°. However, depending on the relative sizes of the *A*-site and *B*-site cations, the system may lower its symmetry, adopting additional atomic displacements and/or octahedral rotations,[1] which may ultimately modify this bond angle. Common examples of distorted perovskites are the orthorhombic and rhombohedral lattices. The orthorhombic lattice is characterized by in-phase octahedral tilts about the longest orthorhombic axis and out-of-phase tilts about the two perpendicular pseudocubic (PC) axes. While, out of six possible space group settings, *Pnma* is the conventional one, here, we choose the *Pbnm* setting (where

Pnma axes ***a***, ***b***, ***c*** are swapped to the order ***c***, ***a***, ***b***), which is commonly used since it gives a conceptual advantage where *Pbnm* c_{ORT} corresponds to the long orthorhombic axis. In comparison, the rhombohedral lattice belongs to the $R\bar{3}c$ space group and has out-of-phase rotations about all three PC axes. In Glazer notation, the octahedral tilt patterns of these two structures are, respectively, described as $a^-a^-c^+$ and $a^-a^-a^-$.[2–4] In conjunction, the *B*–O–*B* bond angle becomes modified. The physical properties of these oxides are, in turn, influenced by the geometry of this bond, as it regulates the orbital overlapping between the 2*p* and *d* electronic levels of the oxygen and transition metal, respectively.[5–8] Tuning this structural parameter is, therefore, a common strategy for tailoring their physical properties.[9–12] This is often done by growing epitaxial heterostructures, where the bond characteristics are modified due to a biaxial strain imposed by the lattice mismatch from the underlying single crystal substrate.[13–15] The characteristic length-scale associated with this strain effect can be rather long (of the order of tens of nanometers), after which it may be partially relieved through the incorporation of lattice defects in the film.[16,17] Over a shorter length-scale range (a few unit cells), this bond angle can be more drastically modified by engineering an epitaxial and coherent interface between two perovskite materials with dissimilar *B*–O–*B* bond angles.[10,18–20] In this scenario, however, other interfacial phenomena such as charge transfer, polar discontinuities, and orbital reconstructions, among others, may also affect the behavior of the heterostructures and, therefore, need to be considered to understand the physical properties of the engineered systems.[21–25] In addition to this, a symmetry mismatch between two neighboring epitaxial oxide layers may also affect the structural properties of the system, spanning over a length-scale intermediate to the two aforementioned contributions.[26–31] An example of this occurs in compounds with *Pbnm* symmetry: the constraint imposed on the deposited film depends on the orientation of the lattice with respect to the underlying substrate. For instance, when the substrate is cubic, the unit cell is shear strained when the long orthorhombic axis (c_{ORT}) is oriented perpendicular to the interface with the substrate ("out-of-plane"), whereas this shear strain does not develop when c_{ORT} lies in the substrate plane ("in-plane").[32,33] As the resulting physical properties of the deposited films may depend on their precise crystallographic orientation and associated structural domain morphology,[27,28,34–36] identifying and controlling these structural parameters is paramount to properly tailoring their physical properties. For instance, this is particularly relevant for engineering improper ferroelectricity in *Pbnm* systems, where an out-of-plane c_{ORT} axis is required.[37–40] Moreover, depending on the crystallographic orientation, distinct multidomain configurations may be present in the films, which can ultimately affect their defect landscape and physical properties.

The crystallographic orientation of *Pbnm* systems can be assessed from the characteristic half-order reflections appearing in x-ray diffraction (XRD) or electron diffractograms.[41–43] However, these techniques do not provide real-space information about their domain characteristics. For this purpose, here, we describe an efficient methodology to map the distribution of *Pbnm* domains and associated boundaries in real space, using scanning transmission electron microscopy (STEM). Our technique is based on the geometrical phase analysis (GPA) algorithm, as commonly used to map strain fields in high-resolution (S)TEM images.[44–46] While GPA is known to be useful for mapping polarization textures in ferroelectric samples—thanks to the large difference between the *a*/*c* parameters in tetragonal systems[47,48] it has not yet been exploited to map *Pbnm* domains, because the three PC lattice parameters are all of similar length in this structure. Despite this fact, here, we show that GPA is still suitable to map the distribution of *Pbnm* domains, by applying specific (and unconventional) virtual aperture settings. After its demonstration, we employ our method on a series of orthorhombic (*Pbnm*) rare-earth nickelate heterostructures grown under different epitaxial constraints. This particular oxide family has been widely studied, because it displays a bandwidth-controlled metal–insulator transition (MIT) that is directly regulated by the Ni–O–Ni bond angle.[6,14,49,50] We propose that the orientation of the crystallographic structure and the resulting domain distribution is set by an energy competition between three contributions: two elastic terms related to epitaxial strain (one component from the normal strain and the other from the shear strain) and an interfacial term that depends on the coupling of octahedral rotations and/or atomic displacements at the interfaces. The methodology described in this work, and all the main conclusions, can be directly transferred to any *Pbnm* system, as well as other systems presenting similar structural distortions or other additional reflections in the Fourier transform patterns of their atomic resolution STEM images.

II. METHODOLOGY DESCRIPTION

The *Pbnm* crystal structure of $NdNiO_3$ is displayed in Fig. 1, viewed along the $[001]_{\mathrm{ORT}}$ (or c_{ORT}) zone axis, panel (a), and the $[1\bar{1}0]_{\mathrm{ORT}}$ zone axis (a_{PC} or b_{PC}), panels (b) and (c). Note that the PC lattice parameters relate to the orthorhombic parameters as follows:

$$a_{\mathrm{PC}} = b_{\mathrm{PC}} = \sqrt{\left(a_{\mathrm{ORT}}^2 + b_{\mathrm{ORT}}^2\right)}/2,$$

$$c_{\mathrm{PC}} = c_{\mathrm{ORT}}/2.$$

Each of the orthorhombic compounds studied here has PC lattice parameters that are very similar to each other, when in its

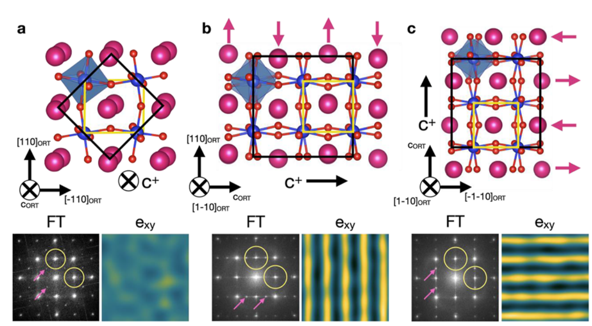

FIG. 1. *Pbnm* crystal structure viewed along the (a) $[001]_{\mathrm{ORT}}$ (c_{ORT}) and [(b) and (c)] $[1\bar{1}0]_{\mathrm{ORT}}$ zone axes. The orthorhombic and pseudocubic unit cells are indicated with black and yellow squares, respectively. The magenta arrows indicate the *A*-site antipolar displacements. The lower panels show (left) the FT patterns obtained from each corresponding domain type in high-resolution STEM images and (right) the associated features seen in the GPA antipolar motion maps when the yellow circles are used as virtual apertures. The pink arrows in the FT diagrams point to the half-order reflections characteristic of each specific *Pbnm* zone axis and lattice orientation.

unstrained state (c_{PC} within 0.1%–0.2% of a_{PC}). This *Pbnm* structure presents an $a^-a^-c^+$ tilt pattern, which means that the oxygen octahedra rotate in-phase (+ sign) and out-of-phase (− sign) about one and two PC axes, respectively. To partially compensate the oxygen octahedral tilts, additional *A*-site (rare-earth, here Nd) displacements appear,[3,4] which run perpendicular to the c_{ORT} axis direction, as shown by the arrows in Figs. 1(b) and 1(c). These *A*-site displacements are commonly referred to as antipolar motion displacements (or X_5^- mode) and are coupled with the octahedral tilts through a trilinear energetic term.[51,52] Depending on the orientation of the *Pbnm* unit cell, these cations can be either displaced vertically or horizontally with respect to the film/surface interface, as in Figs. 1(b) and 1(c), respectively. It is these octahedral tilts and *A*-site displacements that, in the orthorhombic lattice, double the symmetry length compared to the PC lattice along the direction parallel to c_{ORT} (i.e., $c_{ORT} = 2c_{PC}$). In the Fourier transform (FT) patterns shown in the bottom row of Fig. 1, this leads to the appearance of additional Bragg reflections at half-order peak positions, as compared to the primary PC reflections. (Example half-order peaks are indicated by pink arrows.) For comparison, Fig. S1 of the supplementary material presents the selected area electron diffraction (SAED) patterns from a representative *Pbnm* rare-earth compound recorded on the equivalent $[1\bar{1}0]_{ORT}$ and $[001]_{ORT}$ zone axes.

Identifying the reciprocal space positions of these specific half-order reflections in XRD or electron diffractograms, therefore, allows the *Pbnm* crystallographic orientation to be determined.[17,53,54] Moreover, when appropriate aperture settings are chosen (see the yellow circles in the FT patterns of Fig. 1), the GPA of the STEM images detects these antipolar motion displacements as parallel and narrow fringes in the shear (e_{xy}) and rotation (r_{xy}) strain maps when the crystal structure is viewed along the $[1\bar{1}0]_{ORT}$ zone axis [see the bottom panels of Figs. 1(b) and 1(c)]. (Note that we do not show the rotation maps in this article because they are equivalent to the shear strain ones.) Therefore, the presence and orientation of these fringes can be used to retrieve the orientation of the orthorhombic unit cell at each image region.

We now describe, in detail, the reasons behind the appearance of these fringes. We consider a deposited film consisting of several domains with distinct crystallographic orientations. When the acquired high-angle annular dark field (HAADF) image contains at least two of these domains, multiple half-order reflections will be present within its associated FT pattern. A possible strategy to map the spatial distribution of these domains is generating inverse FT images from each set of half-order reflections (each one linked to a particular orientation).[55] An example of this is shown in Fig. 2, where we display several inverse FT images generated using distinct virtual apertures from a high-angle annular dark field (HAADF) STEM image acquired from a $NdNiO_3$ thin film grown on (001)-oriented $LaAlO_3$. Note that, in this case, two distinct domains are present in the image (see the insets), each one generating distinct arrangements of half-order reflections in their associated FT patterns that are like those shown in Figs. 1(a) and 1(b) for the equivalent orientations. Figure 2(b) displays a reconstructed image generated by selecting the $(001)_{PC}$ spots in the FT pattern and performing an inverse FT. The resulting image consists of horizontal parallel fringes that relate to the out-of-plane spacing of the lattice. The same process is repeated in Fig. 2(c); this time selecting only the

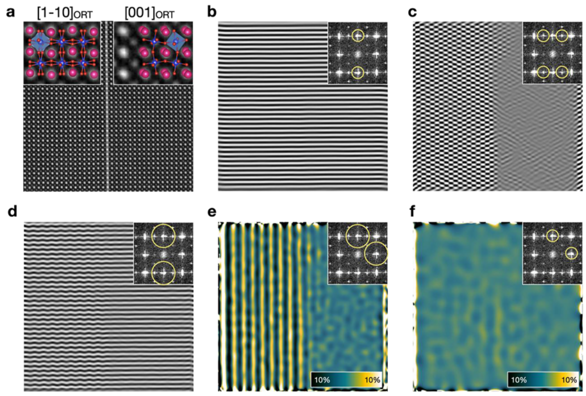

FIG. 2. (a) Atomic-resolution HAADF STEM image acquired from a $NdNiO_3$ thin film deposited on a $(001)_{PC}$-oriented $LaAlO_3$ single crystal substrate. The insets show a magnified view of the film on either side of the image, with an overlaid illustration of the $NdNiO_3$ unit cell projected along the corresponding zone axis (indicated in the upper label). The boundary separating both domains is indicated with a white line. (b)–(d) Inverse FT images generated by using different virtual apertures, indicated with yellow circles in the FT patterns that are included in the insets. A wavy pattern is seen in the left side of panel (d), as correlated with the *A*-site AM displacements of its domain. (e) and (f) Antipolar motion maps generated with GPA using different aperture sizes. Narrow vertical fringes appear in the left side of panel (e) due to the wavy pattern observed in panel (d).

$\left(\frac{1}{2}01\right)$ *and* $\left(\frac{\bar{1}}{2}01\right)$ sets of reflections. Since we have selected two sets of reflections, the reconstructed image consists of the summation of the two individual patterns generated from each set of reflections. Nevertheless, it is clearly seen that the resulting chessboard-like pattern is only present in the left-side region, which corresponds to a $[1\bar{1}0]_{ORT}$ zone axis and so is responsible for generating the two selected reflections in the FT pattern. This methodology enables us to correlate specific reflections in the Fourier space with its corresponding real-space area, thus allowing us to map the distribution of domains with distinct crystallographic orientations. However, since a similar pattern is obtained when the c_{ORT} axis is oriented in-plane and out-of-plane (not shown here), these two orientations are not discriminated when using this methodology.

The strategy to overcome this limitation is to combine this chessboard pattern with the one generated using the $(001)_{PC}$ set of reflections. For this, we employ the GPA. The spatial resolution of the generated maps depends on the virtual aperture size, which for classical strain mapping should only include one reflection in order to avoid artifacts. In contrast, in order to achieve our goal, we go against this paradigm. Specifically, we center our reciprocal masks on the $(100)_{PC}$ and $(001)_{PC}$ spots and use an aperture radius larger than $1/(2c_{PC})$ such that the $\left(\frac{1}{2}01\right)_{PC}$ or $\left(10\frac{1}{2}\right)_{PC}$ reflections (if present) are included within the aperture. Note that, since we employ GPA to map orthorhombic domains instead of evaluating strain fields, the same contrast features are obtained regardless of the reference area. Therefore, when the substrate is not viewed in the HAADF image, in general, we simply use the whole film image as a reference. In order to illustrate this process, in Fig. 2(d), we first display the inverse FT image of the $NdNiO_3$ sample generated using a large virtual aperture that selects both $(001)_{PC}$ *and* $\left(\frac{1}{2}01\right)_{PC}$ reflections. Now, instead of straight lines such as in panel (b), the fringes follow a wave-like pattern in the left-side area. The same pattern is also obtained by summing the filtered images obtained in panels (b) and (c). When we now apply these large virtual aperture settings to the GPA, the wavy features are translated as local (occurring at each PC unit cell) shear (e_{xy}) and rotation (r_{xy}) deformations with alternating signs along the c_{ORT} direction. As a result, in the regions where the lattice is viewed along the $[1\bar{1}0]_{ORT}$ zone axis, the resulting shear and rotation maps consist of narrow and parallel fringes oriented perpendicular to the c_{ORT} axis. This outcome is seen in the left domain of Fig. 2(e), which shows the antipolar motion map made using this method. Note that the fringes appearing in the antipolar motion maps do not correspond to real strain deformations, as they relate to the intrinsic antipolar motion displacements of the *A* cations. Therefore, from now on, we will refer to these maps as antipolar motion maps. In accordance with the principle behind our methodology, reducing the aperture radius below $1/(2c_{ORT})$ (as conventional for GPA) makes these fringes disappear, as shown in Fig. 2(f). It should be remarked that, even though these fringes are not present in domains viewed along the c_{ORT} zone axis, we can still distinguish the *Pbnm* symmetries from the other perovskite lattices, e.g., cubic, tetragonal, and rhombohedral, because this c_{ORT} zone axis still presents some specific and characteristic half-order reflections in the associated FT pattern, as displayed in Fig. 1(a). These reflections arise from the projection of the antipolar displacements of the *A*-site columns. As a result, the atomic columns are elongated along either the $[101]_{PC}$ or the $[\bar{1}01]_{PC}$ direction in an alternating pattern, giving rise to additional peaks corresponding to the $\{1/2\ 0\ 1/2\}_{PC}$ family of planes.

In the following, we apply our method to a series of rare-earth nickelate heterostructures in order to unravel correlations between distinct epitaxial constraints and their resulting domain distributions. We note that various studies use *A*-site antipolar displacements as a proxy for measuring orthorhombic orientation/distortion, by quantifying the displacements through real-space tracking of cation column positions.[54,56–58] From the *A*-site positions, Meley *et al.* further calculated virtual shear strain maps to give fringes analogous to those presented here.[59] In comparison, the adapted GPA that we present here (and that we first applied in Fowlie *et al.*[60]) is more akin to the GPA-based method used to visualize longer-range (many unit cell) charge ordering in $La_{0.6}Sr_{2.4}Mn_2O_7$ Ruddlesden–Popper compounds in the supporting information of Zheng *et al.*[61] Critically, by working in Fourier space and by removing the need to identify each *A*-site column, this method is both fast and easily capable of handling images containing large numbers of atomic columns. We find that it is also robust to moderate scan noise and distortions. Indeed, taking advantage of these factors, on other systems, we regularly apply the technique to low-quality, low magnification (640 kx nominal) 8k × 2k pixel images containing ~60 000 *A*-site columns. In our case, we apply the method using the freely available DigitalMicrograph plugin FRWRTools. Since, even for large, 16 megapixel scan images, the calculation is performed in a few tens of seconds, we can integrate its use into the workflow at the microscope, for instance using it to identify domain boundaries or interesting defects, as described later and in the supplementary material. From inspection of e_{xy} noise and from consideration of the STEM-GPA analysis by Zhu *et al.*,[45] we estimate that the limit of detectability will be projected antipolar displacements of $\lesssim\pm 2$ pm—well below that of the X_5^- mode in typical *Pbnm* perovskite oxides. Recently, Goodge *et al.* introduced the "phase lock-in" approach as a fast algorithm for the real-space characterization of structural defects in crystalline materials, as applied to perovskite oxides.[56] We show how adapted GPA also gives real-space visualization and insights into common defects present in *Pbnm* materials.

III. MAPPING *Pbnm* DOMAINS IN $NdNiO_3$ THIN FILMS

We now use the methodology described in Sec. II to study the distribution of *Pbnm* domains in $NdNiO_3$ thin films grown on $(001)_{PC}$-oriented $LaAlO_3$, $(LaAlO_3)_{0.3}$–$(Sr_2AlTaO_6)_{0.7}$ (LSAT) and $SrTiO_3$, as well as $(110)_{ORT}$-oriented [$\equiv(001)_{PC}$-oriented] $NdGaO_3$ single crystal substrates. All the studied films have an approximate thickness of 15–20 nm. As the different substrates impose varying degrees of epitaxial strain on the $NdNiO_3$ films, in Table I, we display the calculated strain tensors for $NdNiO_3$ growth on each of them, for the three possible film orientations. Strain tensors were determined using the methods described in the section "Strain state calculations" of the supplementary material.

TABLE I. Strain tensor components associated with the crystallographic deformation of the $NdNiO_3$ unit cell when grown on $LaAlO_3$, LSAT, $SrTiO_3$, and $NdGaO_3$ for the three possible film orientations. a_{PC} and b_{PC} are parallel to the substrate surface, and c_{PC} is perpendicular to it.

Film orientation	$LaAlO_3$	LSAT	$SrTiO_3$	$NdGaO_3$ (*Pbnm*, $c_{ORT}\|\|b_{PC}$)
$c_{ORT}\|\|a_{PC}$	$e_{xx} = -0.47\%$ $e_{yy} = -0.40\%$ $e_{xy} = 0\%$	$e_{xx} = 1.65\%$ $e_{yy} = 1.73\%$ $e_{xy} = 0$	$e_{xx} = 2.55\%$ $e_{yy} = 2.63\%$ $e_{xy} = 0$	$e_{xx} = 1.53\%$ $e_{yy} = 1.22\%$ $e_{xy} = 0$
$c_{ORT}\|\|b_{PC}$	$e_{xx} = -0.40\%$ $e_{yy} = -0.47\%$ $e_{xy} = 0\%$	$e_{xx} = 1.73\%$ $e_{yy} = 1.65\%$ $e_{xy} = 0$	$e_{xx} = 2.63\%$ $e_{yy} = 2.55\%$ $e_{xy} = 0$	$e_{xx} = 1.45\%$ $e_{yy} = 1.30\%$ $e_{xy} = 0$
$c_{ORT}\|\|c_{PC}$	$e_{xx} = -0.47\%$ $e_{yy} = -0.47\%$ $e_{xy} = -0.14\%$	$e_{xx} = 1.65\%$ $e_{yy} = 1.65\%$ $e_{xy} = -0.07\%$	$e_{xx} = 2.55\%$ $e_{yy} = 2.55\%$ $e_{xy} = -0.07\%$	$e_{xx} = 1.45\%$ $e_{yy} = 1.22\%$ $e_{xy} = -0.07\%$

To evaluate the domain distribution in these systems, we have recorded high-resolution HAADF STEM images of the film cross sections, as shown in the left panels of Fig. 3, and then applied our GPA-based approach to generate their corresponding antipolar motion maps, as shown in the right panels of the same figure.

Considering the strain values presented in Table I, one could expect that compressive strain will favor an in-plane c_{ORT} axis orientation, whereas tensile strain will stabilize the out-of-plane c_{ORT} direction, since, in both cases, this would minimize the normal strain. First looking at the compressive case of the $NdNiO_3/LaAlO_3$ system, its results are in agreement with expectations. In its antipolar motion map, shown in the right panel of Fig. 3(a), we identify two different kinds of contrast, both corresponding to domains with the c_{ORT} axis oriented in-plane but with this axis either perpendicular (vertical fringes) or parallel (no fringes) to the viewing axis. This outcome is in agreement with previous reports,[32,42] with c_{ORT} of the film orienting in-plane in order to minimize epitaxial strain. The two different lattice orientations that are observed for this c_{ORT} in-plane configuration result from the equivalence of a_{PC} and b_{PC} in the $LaAlO_3$ substrate such that domains are equally likely to grow with c_{ORT} parallel to a_{PC} or b_{PC} of $LaAlO_3$. While these basic orientations can also be found with XRD, the STEM-GPA analysis allows us to visualize the domain sizes, which are observed to be rather small (from tens to hundreds of nanometers). The domains are separated by abrupt vertical boundaries, which have an approximate width of one PC unit cell, ~0.4 nm. As we will show later using plan-view imaging, these boundaries run along the $[110]_{PC}$ direction. Therefore, in the cross section, they sometimes appear to be slightly wider, owing to a projection effect as they are consequently angled by 45° to the incident electron beam.

We now turn to the tensile strain scenario, as applied by the other three substrates. First looking at the results acquired on the $NdNiO_3/SrTiO_3$ system in Fig. 3(b), in its antipolar motion map, we observe only one kind of contrast—horizontal fringes. This corresponds to an out-of-plane c_{ORT} orientation, as expected for the strain state. However, when we repeat the analysis on the $NdNiO_3$/LSAT heterostructure, as shown in Fig. 3(c), the scenario is more complex. Strikingly, despite the imposed tensile strain, all three possible crystallographic orientations are found to co-exist in the same film, with most domains actually having an in-plane c_{ORT} axis. While a similar multidomain configuration has been reported in other *Pbnm* systems,[42] we point out the ease with which our GPA-based technique directly samples the spatial distribution of the domains. To help interpret these results, we further note that the contrast observed in the LSAT substrate area of the antipolar motion map of Fig. 3(c) is similar to that of the background noise (as observed in the vacuum region above the lamella). This occurs because the intensity of the $(100)_{PC}$ reflections almost vanishes in the LSAT substrate since both *A*-site and *B*-site columns present similar brightness.

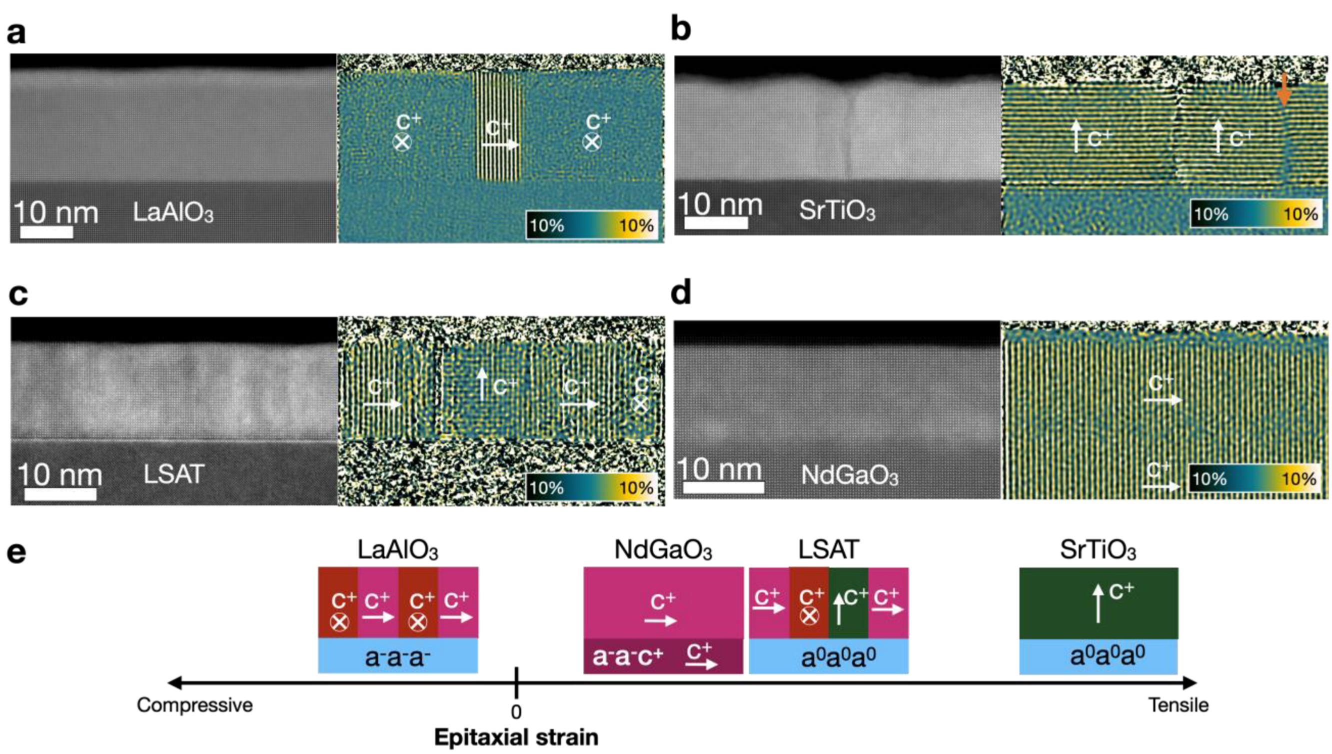

FIG. 3. HAADF images (left) and associated antipolar motion maps (right) acquired from $NdNiO_3$ films grown on $(001)_{PC}$-oriented (a) $LaAlO_3$, (b) $SrTiO_3$, and (c) LSAT single crystal substrates. The orange arrow points to a twin (or possibly antiphase) boundary. (d) HAADF image (left) and associated antipolar motion map (right) acquired in $NdNiO_3$ films grown on $(110)_{ORT}$-oriented $NdGaO_3$. (e) Illustration showing the evolution of the lattice orientation and associated domain distribution with epitaxial normal strain.

While the tensile strain imposed on this film may make the observed mixture of domain orientations appear unlikely, the full set of imposed strain values in Table I provides a possible explanation. If c_{ORT} is oriented out-of-plane, a finite e_{xy} shear deformation is imposed. This occurs because $[1\bar{1}0]_{\mathrm{ORT}}$ and $[110]_{\mathrm{ORT}}$ of the film are now constrained to be parallel to the *a* and *b* axes of the cubic LSAT substrate, i.e., they are orthogonal, which is not the case in the free-standing *Pbnm* crystal structure. Therefore, even if the tensile strain is smaller when c_{ORT} is oriented out-of-plane, this is counterbalanced by the ability to relax the e_{xy} shear strain by, instead, orienting c_{ORT} in-plane. Evidentially, this leads to a competition between the growth of either c_{ORT} orientation when the tensile strain is applied by a cubic substrate. Comparison with the results of growth on cubic $SrTiO_3$, which applies a greater tensile strain and for which only c_{ORT} out-of-plane is observed, indicates that the complete epitaxial orientation transition from in-plane to out-of-plane c_{ORT} axis occurs at a non-zero tensile strain value. Moreover, the fact that all three possible orientations co-exist in the same film indicates that this transition is not abrupt but gradual, with the nucleation energy for all the three crystallographic orientations being similar. These results point to the importance of considering more than just the applied compressive/tensile strain to *Pbnm* film growth in determining resultant film orientation, which could be interesting to study further by recourse to first-principles calculations, as, for instance, was made by Meley *et al.* on strained $LaVO_3$ films.[59]

Such additional considerations come to the fore in the last $NdNiO_3$ film studied in this section, which was grown on (110)-oriented $NdGaO_3$; see Fig. 3(d). As can be observed in its antipolar motion map, we only observe one domain in this film, with the vertical fringes indicating a solely in-plane c_{ORT} axis orientation, even though $NdGaO_3$ imposes similar tensile and shear strain values to the LSAT substrate, which demonstrated a mixed domain configuration. The difference here is that the $NdGaO_3$ substrate and $NdNiO_3$ film share a *Pbnm* symmetry; as a result, the substrate imprints its crystallographic orientation onto the $NdNiO_3$ film because of the structural couplings established at the film/substrate interface. This coupling has been observed in other systems where the substrate and the film similarly present the same *Pbnm* symmetry.[27,31,42]

The mechanism behind such an imprinting of substrate symmetry and hence orientation onto the film is understood to be the minimization of local structural mismatch at the interface, in terms of the key orthorhombic distortions of octahedral tilt pattern and *A*-site displacements. Therefore, in addition to the considerations of epitaxial normal and shear strain, an additional term linked to the structural couplings at the interface (interfacial energy) may also need to be considered for understanding film orientation. Calculating this interfacial cost for the systems studied here is a nontrivial task; however, we mention that the phenomenology of such a *Pbnm*/*Pbnm* interface is studied with second-principles modeling in Alexander *et al.*[58] Interestingly, we could not find any lattice defects in this film, which we attribute to its monodomain nature resulting from the uniform lattice orientation. Note that this differs to the $NdNiO_3/SrTiO_3$ system. While, in the latter system, we also observe an out-of-plane c_{ORT} axis orientation, the film may contain twin boundaries separating domains with reversed tilt patterns. For example, the crystallographic defect observed in Fig. 3(b), which is indicated with an orange arrow, could be one of these twin boundaries. The zig-zag pattern of the *A*-site cations (antipolar motion displacement also linked to the $a^-a^-c^+$ tilt pattern) is inverted on either side of this boundary, which is precisely what we would expect when a_{ORT} and b_{ORT} are swapped. However, we cannot rule out either the possibility of this boundary being an antiphase boundary—where the atomic structure jumps by $c_{\mathrm{ORT}}/2$ along the c_{ORT} axis—as on this structural projection it would present the same behavior for the *A*-site and *B*-site sublattices. No such twin (or antiphase) boundaries are observed in the $NdNiO_3/NdGaO_3$ system, stemming from its monodomain configuration that is driven by the substrate symmetry. In comparison, the cubic substrate of the $NdNiO_3/SrTiO_3$ system has no such influence, such that the film can nucleate domains with a_{ORT} parallel to either in-plane unit cell diagonal of the substrate. In addition to locating twin/antiphase boundaries, we point out that our methodology is also well-suited for identifying characteristic stacking faults where the antipolar zig-zag displacements are locally suppressed. Figure S2(a) of the supplementary material shows an example, where a stacking fault that is barely noticeable in the raw HAADF-STEM image is rendered obvious using our methodology (even at low STEM magnifications), as the width of the fringe generated in the associated e_{xy} strain map increases by a factor of two at the fault. As shown in the inset, a closer inspection of the HAADF image reveals that the zig-zag displacements are canceled at this location.

Beyond such planar defects, we note that other defects are also present in the rare-earth nickelate films shown in Fig. 3. While, in most of the cases, these correspond to Ruddlesden–Popper faults, the most common defect observed in rare-earth nickelate heterostructures,[62] some misfit dislocations are also identified in the film grown on $SrTiO_3$. A more detailed discussion about the correlation between lattice orientation and defect landscape is given in Sec. IV.

To summarize this section, as illustrated in the chart of Fig. 3(e), we observe that the crystallographic orientation of *Pbnm* films grown on substrates with cubic cation sublattices (i.e., $LaAlO_3$, LSAT, and $SrTiO_3$) is determined by an energetic competition between in-plane normal and shear strain. Under compressive strain, the c_{ORT} axis is oriented in plane, and it changes to an out-of-plane orientation as tensile strain is increased beyond a non-zero value, with both orientations co-existing near the orientation transition. Usefully, our GPA-based approach readily identifies the location of domain boundaries, even when they are difficult to detect visually in the associated HAADF images, such as the apparent twin boundary in Fig. 3(b). The different types of domain boundaries may, in turn, present novel functional properties arising from the structural couplings that need to be established to connect the octahedral tilt patterns between the neighboring domains.

IV. DOMAIN DISTRIBUTION IN $Nd_{1-x}La_xNiO_3$ SOLID-SOLUTION THIN FILMS

Given the strong apparent effect of an otherwise subtle competition between tensile and shear strain on the film orientation and domain landscape, it is interesting to study this balance further. However, experimentally, it is challenging to gradually modify the applied epitaxial strain by changing substrates. Therefore, we, instead, investigate this energetic competition by introducing a certain fraction of La onto the *A*-sites of the film, through a series of $Nd_{1-x}La_xNiO_3$ solid-solution thin films deposited on (001)-oriented

LSAT single crystal substrates. By progressively increasing the La/Nd ratio, we can gradually change both strain components, all the while maintaining a tensile strain state. Specifically, here, we analyze two films having relative La concentrations of $x = 0.1$ and $x = 0.3$ deposited on LSAT substrates and later compare two other films, both with $x = 0.4$, deposited on LSAT and $NdGaO_3$ substrates, respectively. We do not go beyond this La content because, above $x = 0.4$, orthorhombic and rhombohedral phases co-exist in the same film, as previously reported.[60] Figures 4(a) and 4(d) present the HAADF images of the films with $x = 0.1$ and $x = 0.3$, respectively.

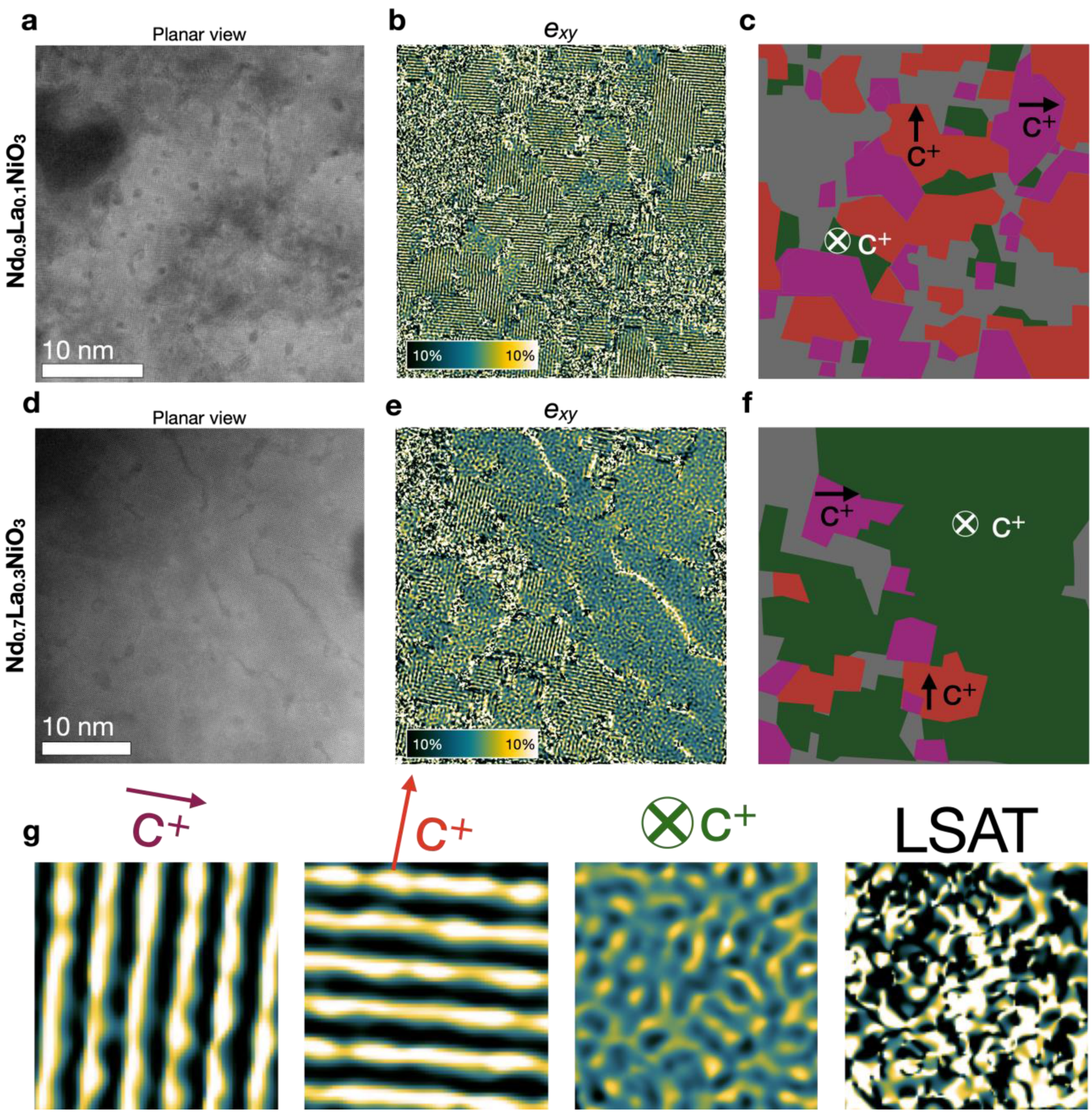

FIG. 4. Plan-view HAADF image acquired in (a) a $Nd_{0.9}La_{0.1}NiO_3$ and (d) a $Nd_{0.7}La_{0.3}NiO_3$ solid-solution thin film grown on LSAT. Their associated antipolar motion maps are presented in (b) and (e), respectively. (c) and (f) Orthorhombic domain distribution maps obtained from the antipolar motion maps displayed in (b) and (e). Each contrast feature, as all shown in (g), is indicated with a different color. The gray areas correspond to the LSAT regions.

Unlike the previous analyses made using cross section views, the STEM samples have been prepared in a plan-view geometry, which offers both a larger overview of the domain distributions, while also being free of the stereological limitations of a cross section sample with regard to the sampling of domain sizes.

As before, we apply our GPA-based approach to map their orthorhombic domain distributions. The antipolar motion maps are presented in panel (b) for $x = 0.1$ and panel (e) for $x = 0.3$. These maps clearly reveal the same contrast features linked to the *A*-site antipolar displacements as before. Given the large field of view of the input images, this is a clear demonstration of the robustness of our methodology. Because of the change in sample geometry, domains with parallel fringes now correspond to c_{ORT} in-plane. No fringes are observed for c_{ORT} out-of-plane, because the c_{ORT} axis is now parallel to the viewing axis. Usefully, however, as shown in panel (g), the residual contrast for the c_{ORT} out-of-plane domains is different from that of the LSAT substrate, whose similar atomic numbers for the *A*- and *B*-sites give it a different color on the antipolar motion map, as described previously. This allows the two to be discriminated in the antipolar motion maps. The presence of isolated regions of the LSAT substrate in the images likely relates to damage induced by the ion milling process during STEM specimen preparation, as it may entirely remove the film in these areas because of the film's low thickness (15–20 nm). To facilitate the interpretation of the antipolar motion maps, we have colored the areas belonging to the distinct contrast features with different colors representing *Pbnm* domains of the three possible orientations, or substrate area. The resulting sketches are shown in Figs. 4(c) and 4(f) for the $x = 0.1$ and $x = 0.3$ cases, respectively. Even though we see the co-existence of domains with either in-plane or out-of-plane c_{ORT} axis orientation in both films, a clear evolution of their proportions is identified when comparing them. While most domains present the in-plane c_{ORT} axis (magenta and red colors) in the $x = 0.1$ film (like in the pure $NdNiO_3$ thin film), the opposite situation is found in the $x = 0.3$ film, with most domains being oriented with the c_{ORT} axis out-of-plane (green color).

To understand this evolution, we have calculated the strain tensors for pure $NdNiO_3$—using it as a close proxy for the $x = 0.1$ film—and for an $Nd_{0.7}La_{0.3}NiO_3$ single crystal constrained to an LSAT $(100)_{PC}$-oriented substrate. Table II displays the resultant e_{xx}, e_{yy}, and e_{xy} values for the epitaxial growth of $NdNiO_3$ and $Nd_{0.7}La_{0.3}NiO_3$ on LSAT. Comparison of these values implies that, as La concentration increases in a $Nd_{1-x}La_xNiO_3$ solid solution, the tensile strain will decrease, while, for the $c_{ORT}||c_{PC}$ orientation, the shear strain will increase. Given our hypotheses in Sec. III, whether considering applied tensile strain or applied shear strain, one would, therefore, expect a decrease in the fraction of c_{ORT} axis out-of-plane when x is increased.

TABLE II. Strain tensor components associated with the crystallographic deformation of the $NdNiO_3$ and $Nd_{0.7}La_{0.3}NiO_3$ unit cells, when grown on LSAT with the two basic possible film orientations. (Note that $c_{ORT}||b_{PC}$ gives the same values as $c_{ORT}||b_{PC}$, except with e_{xx} and e_{yy} exchanged.) For $Nd_{0.7}La_{0.3}NiO_3$, we have used the lattice constants of bulk $Nd_{0.7}La_{0.3}NiO_3$ single crystals that were measured by Medarde *et al.*[63]

c_{ORT} orientation	$NdNiO_3$	$Nd_{0.7}La_{0.3}NiO_3$
$c_{ORT}\|\|a_{PC}$ or $c_{ORT}\|\|b_{PC}$	$e_{xx} = 1.65\%$ $e_{yy} = 1.73\%$ $e_{xy} = 0$	$e_{xx} = 1.32\%$ $e_{yy} = 1.45\%$ $e_{xy} = 0$
$c_{ORT}\|\|c_{PC}$	$e_{xx} = 1.65\%$ $e_{yy} = 1.65\%$ $e_{xy} = -0.07\%$	$e_{xx} = 1.32\%$ $e_{yy} = 1.32\%$ $e_{xy} = -0.37\%$

In contrast, Fig. 4 shows that, experimentally, we find the opposite. However, the situation here is a bit more complex because, as we observe all three possible crystallographic orientations in both films, their epitaxial strain is probably close to the crossover point and, hence, the domain distribution may be very sensitive to any structural modulation. Moreover, we believe that the key to understanding the observed and surprising domain evolution is to consider not only the average tensile strain, but the difference in strain when swapping the c_{ORT} axis from in-plane to out-of-plane. While in both cases (necessarily), e_{xx} does not change when going from c_{ORT} axis in-plane to out-of-plane, e_{yy} decreases by 0.08% for the $NdNiO_3$ case but a much larger 0.13% for the $Nd_{0.7}La_{0.3}NiO_3$ case. This is because the shape of the pseudocubic unit cell is almost cubic for bulk $NdNiO_3$ but becomes more distorted for both decreasing and increasing sizes of the *A* cation.[6] Note that this does not imply that atomic displacements within the unit cell are minimal for $NdNiO_3$. As the La content increases, the difference between pseudocubic lattice parameters increases and the angle between $[1\bar{1}0]_{ORT}$ and $[110]_{ORT}$ (which is related to the difference between a_{ORT} and b_{ORT}) departs farther from 90°. Thus, while the energy cost associated with shear strain favors c_{ORT} in-plane more strongly for $x = 0.3$ than for $x = 0.1$ ($\cong NdNiO_3$), the cost due to normal strain, counter-intuitively, favors c_{ORT} out-of-plane more strongly for $x = 0.3$ than for $x = 0.1$. Our observation that there are more domains with c_{ORT} out-of-plane in the case of $x = 0.3$ indicates that the latter effect is the stronger of the two. In addition, to predict the domain distribution in each film, we should also consider the interfacial term associated with the structural couplings, as the amplitude of the structural distortions linked to the *Pbnm* structure decreases with La content x, although this goes beyond the scope of this work.[54]

Beyond giving a detailed overview of the domain distributions, the plan-view images and antipolar motion maps also enable a direct analysis of the domain boundary orientations, which could not be achieved in the cross section data given the projection effect on these vertical boundaries. This is demonstrated in Fig. 5(a), which presents an amplified view of the HAADF image of the $Nd_{0.9}La_{0.1}NiO_3$ film shown in Fig. 4(a) and its corresponding antipolar motion map. It is seen that the boundaries separating domains with an in-plane c_{ORT} axis orientation run along the $[110]_{PC}$ direction, as previously stated. In addition to the domain boundaries, lattice defects, specifically Ruddlesden–Popper faults (RPFs), are also observed in the data. In the antipolar motion map, these faults are seen as straight dark or bright lines, each of which is associated with a structural shift of the lattice by half a PC unit cell along the $[111]_{PC}$ direction. RPFs are commonly observed in rare-earth nickelates.[16,17,62,64] In Fig. 5(a), several RPFs are indicated with red arrows; it is seen that they coincide with the domain boundaries.

Given the observed coincidence of RPFs with domain boundaries, it could be suggested that the density of lattice defects will depend on the domain distribution. In order to study this hypothesis, Figs. 5(b) and 5(c) show the comparison of the cross-sectional

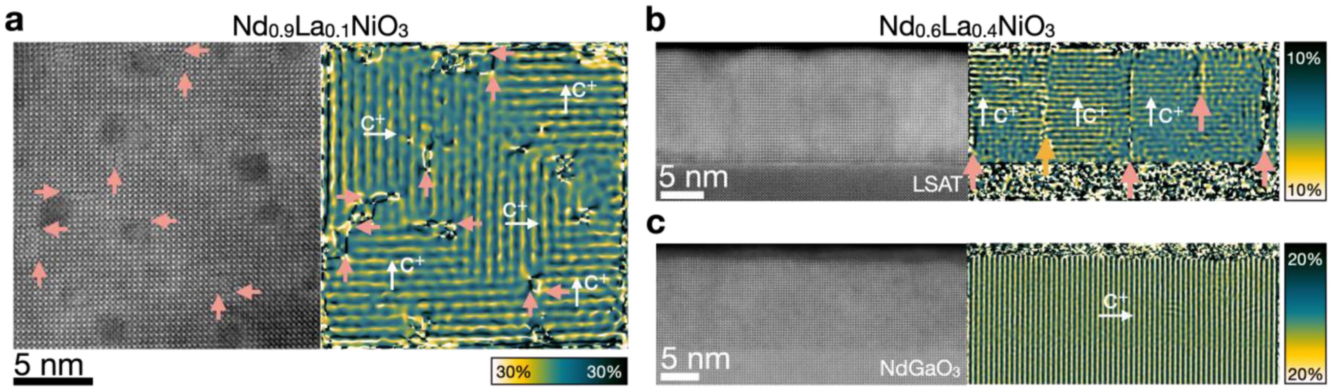

FIG. 5. (a) Amplified view of a central region of the HAADF plan-view image and associated antipolar motion map displayed in Fig. 4(a), which was acquired from a $Nd_{0.9}La_{0.1}NiO_3$ solid-solution thin film deposited on $(001)_{PC}$-oriented LSAT. The red arrows point to RPFs present in the film, which tend to be localized at the boundaries between domains. (b) Cross-sectional HAADF image and associated antipolar motion map acquired from a $Nd_{0.6}La_{0.4}NiO_3$ solid-solution thin film deposited on $(001)_{PC}$-oriented LSAT. The red arrows similarly point to RPF defects, while the orange arrow points to a twin (or antiphase) boundary. (c) Cross-sectional HAADF image and associated antipolar motion map acquired from a $Nd_{0.6}La_{0.4}NiO_3$ solid-solution thin film deposited on $(110)_{ORT}$-oriented $NdGaO_3$. c_{ORT} is oriented along the in-plane direction, evidencing that the orientation of the lattice rotates by 90°, despite the similar strain values imposed by LSAT and $NdGaO_3$.

HAADF images and antipolar motion maps from films grown with the same $Nd_{0.6}La_{0.4}NiO_3$ (x = 0.4) composition but on two different substrates, LSAT and $NdGaO_3$, respectively. Following the tendency of the x = 0.1 and x = 0.3 films shown in Fig. 4, the film grown on LSAT is primarily composed of domains with c_{ORT} out-of-plane. As indicated by the red arrows in Fig. 5(b), many RPFs are again observed at the domain boundaries. A twin (or antiphase) boundary is also seen, as indicated by the orange arrow. This high density of defects contrasts strongly with the data recorded from the $Nd_{0.6}La_{0.4}NiO_3$ film grown on $[110]_{ORT}$-oriented $NdGaO_3$, as shown in Fig. 5(c). As for the pure $NdNiO_3$ grown on this substrate shown in Fig. 3(d), the film has a monodomain nature with an in-plane c_{ORT} axis. Tied to this monodomain nature, it contains no apparent lattice defects. This absence of lattice defects, as compared to the solid-solution film grown on LSAT, is found even though the two films have been grown under the same conditions and have a similar lattice parameter mismatch with the substrate. Therefore, we speculate that the presence of the RPFs in the films grown on LSAT is linked to elastic strain that accumulates at the domain boundaries, which is, in turn, associated with the anisotropy in the *Pbnm* structure and the structural mismatch (of the octahedral tilts and A-site antipolar displacements) between neighboring domains. Our finding, therefore, shows that the defect landscape of nickelate films can be controlled by choosing an appropriate substrate, one that either minimizes or enhances the density of domains. Such a strategy is of interest because, on the one hand, improving the crystal quality of films by decreasing the density of RPFs is key to achieving and enhancing the superconducting properties of reduced (infinite-layer) nickelate films,[65] while, on the other hand, promoting the presence of RPFs can be of interest in some scenarios, such as improving their electrocatalytic properties.[16,64]

V. GENERALITY OF ADAPTED GPA FOR VISUALIZING PERIODIC DISTORTIONS

Throughout this paper, we have focused on mapping *Pbnm* domains imaged along the $[1\bar{1}0]_{ORT}/[010]_{PC}$ zone axis, making use of the X_5^- antipolar mode. This mode consists of A-site displacements parallel to $[010]_{ORT}$, lying within the $(100)_{ORT}$ plane; therefore, our method can equally be applied to visualizing this mode by creating parallel fringes for domains oriented on the $[100]_{ORT}$ zone axis as shown in Fig. S2(b) of the supplementary material. On the corresponding $[110]_{PC}$ axis, this allows such a domain to be readily distinguished from the other two possible orthorhombic orientations of $[010]_{ORT}$ and $\langle 1\bar{1}1\rangle_{ORT}$, which do not show fringes. However, even in reciprocal space, these other two possibilities have strong similarities, and distinguishing them from each other requires analysis of more subtle features, such as observation of closely spaced A-site dumbbells and/or non-orthogonality in the PC lattice of $\langle 1\bar{1}1\rangle_{ORT}$, or a low-angle first-order Laue zone ring that exists for $\langle 1\bar{1}1\rangle_{ORT}$ but not $[010]_{ORT}$.[58]

Going beyond *Pbnm*, our method should also be applicable to other space groups that give superlattice reflections associated with periodic structural distortions. One example is the orthorhombic *Cmcm* space group (having $a_{ORT} \approx b_{ORT} \approx c_{ORT} \approx 2a_{PC}$), whose $a^0b^+b^-$ rotation set also has the X_5^- mode, just at low amplitudes.[3,4,52] Likely more interesting, however, is using it to detect other periodic distortions occurring beyond the scale of the unit cell, such as charge ordering in antiferroelectrics. Commonly, this is measured using tracking of individual atomic columns;[61,66,67] however, if the atomic displacements are periodic such that they generate $(1/n)$ additional reflections in the FT patterns that can be included in the virtual aperture (n being a real number), the displacements can be visualized as parallel fringes using this adaptation of GPA (as, indeed, demonstrated in the supporting information of Zheng *et al.*[61]). In Fig. S3 of the supplementary material, we demonstrate this utilization by visualizing similar atomic displacements as those observed by Jiang *et al.*[66] that generate (1/3) periodic reflections along the $(101)_{PC}$. In our case, these distortions are observed when reducing a $SmNiO_3$ film grown on $NdGaO_3$.[68] Such an ordering is seen in the e_{xy} map, by virtue of being analogous to a lattice shear. If, instead, there is a systematic lattice expansion or contraction beyond the scale of the unit cell, this will also be visualized but, instead, within e_{xx} and/or e_{yy} maps, as demonstrated in Fig. S4 of the supplementary material using a plan-view sample of $SrCuO_{2+\delta}$.[69] These periodic distortions are not readily obvious in standard GPA maps, thereby illustrating how the inclusion of (1/*n*) superlattice reflections within the GPA mask gives a powerful ability to identify subtle periodic variations in an atomic structure.

VI. SUMMARY

In summary, we have presented an efficient tool to map the lattice orientation in *Pbnm* epitaxial heterostructures and their corresponding defect landscape, by using an adaptation of GPA. We have exploited our method to map the domain distributions found in a series of rare-earth nickelate heterostructures. This has, in turn, allowed us to identify that the orientation of the orthorhombic unit cell depends on a competition between in-plane normal and shear strain and also interfacial energy (mismatch of orthorhombic distortions from substrate to film). While only an in-plane c_{ORT} axis is observed in compressed films, split between the domains of the two possible orientations, the three possible in-plane and out-of-plane c_{ORT} lattice orientations are identified in the tensile cases. Further work could be envisaged where these various effects are studied theoretically using first- or second-principles simulations. Given that *Pbnm* is the most common space group for perovskite compounds, our method can, therefore, be widely applied to investigating strain and coupling effects on epitaxial heterostructures, bringing insights that will help in the overall quest for engineering novel systems with enhanced functionalities, ranging from unconventional superconductors to electrochemical catalysts. Finally, we emphasize that our approach is fast and robust and is not only suitable for studying the crystallographic orientation of *Pbnm* systems but also for visualizing any kind of atomic displacements (or spacings) that generate (1/*n*) additional reflections in the Fourier-transform patterns (*n* being a real number).

SUPPLEMENTARY MATERIAL

The supplementary material contains Selected Area Electron Diffraction (SAED) patterns obtained from an example orthorhombic *Pbnm* single crystal substrate, examples where we apply our adaptation of GPA to visualize other lattice distortions or defects, and methods used to calculate the strain state of the epitaxial films on different substrates.

ACKNOWLEDGMENTS

This work was partly supported by the Swiss National Science Foundation through Division II, Grant No. 200020_179155. The research leading to these results received funding from the European Research Council under the European Union's Seventh Framework Program (Grant No. FP7/2007-2013)/ERC Grant Agreement No. 319286 Q-MAC. We acknowledge access to the electron microscopy facilities at the Interdisciplinary Centre for Electron Microscopy (CIME), École Polytechnique Fédérale de Lausanne.

AUTHOR DECLARATIONS

Conflict of Interest

The authors have no conflicts to disclose.

Author Contributions

Bernat Mundet: Conceptualization (lead); Data curation (lead); Formal analysis (lead); Investigation (lead); Methodology (lead); Writing – original draft (lead); Writing – review & editing (lead). **Marios Hadjimichael**: Investigation (supporting); Visualization (supporting); Writing – review & editing (supporting). **Jennifer Fowlie**: Investigation (supporting); Visualization (supporting); Writing – review & editing (supporting). **Lukas Korosec**: Investigation (supporting); Writing – review & editing (supporting). **Lucia Varbaro**: Investigation (supporting). **Claribel Dominguez**: Investigation (supporting). **Jean-Marc Triscone**: Funding acquisition (lead); Investigation (supporting); Writing – review & editing (supporting). **Duncan T. L. Alexander**: Investigation (equal); Methodology (equal); Supervision (equal); Visualization (equal); Writing – review & editing (equal).

DATA AVAILABILITY

The data that support the findings of this study are available at Yareta repository upon reasonable request.

NOMENCLATURE

FT	Fourier transform
GPA	Geometrical phase analysis
HAADF	High angle annular dark field
LSAT	$(LaAlO_3)_{0.3}$–$(Sr_2AlTaO_6)_{0.7}$
ORT	Orthorhombic
PC	Pseudocubic
RPFs	Ruddlesden–Popper faults
STEM	Scanning transmission electron microscopy
TEM	Transmission electron microscopy

REFERENCES

[1] V. M. Goldschmidt, "Die Gesetze der Krystallochemie," Naturwissenschaften **14**, 477–485 (1926).

[2] A. M. Glazer, "The classification of tilted octahedra in perovskites," Acta Crystallogr., Sect. B: Struct. Crystallogr. Cryst. Chem. **28**(11), 3384–3392 (1972).

[3] P. M. Woodward, "Octahedral tilting in perovskites. I. Geometrical considerations," Acta Crystallogr., Sect. B: Struct. Sci. **53**(1), 32–43 (1997).

[4] P. M. Woodward, "Octahedral tilting in perovskites. II. Structure stabilizing forces," Acta Crystallogr., Sect. B: Struct. Sci. **53**(1), 44–66 (1997).

[5] D. Treves, M. Eibschütz, and P. Coppens, "Dependence of superexchange interaction on Fe^{3+} O^{2-} Fe^{3+} linkage angle," Phys. Lett. **18**(3), 216–217 (1965).

[6] L. Medarde, "Structural, magnetic and electronic properties of $RNiO_3$ perovskites (R = rare earth)," J. Phys.: Condens. Matter **9**, 1679–1707 (1997).

[7] P. G. De Gennes, "Effects of double exchange in magnetic crystals," Phys. Rev. **118**(1), 141–154 (1960).

[8] O. Chmaissem, B. Dabrowski, S. Kolesnik, J. Mais, D. E. Brown, R. Kruk, P. Prior, B. Pyles, and J. D. Jorgensen, "Relationship between structural parameters and the Néel temperature in $Sr_{1-x}Ca_xMnO_3$ ($0 \le x \le 1$) and $Sr_{1-y}Ba_yMnO_3$ ($y \le 0.2$)," Phys. Rev. B **64**(13), 134412 (2001).

[9] Z. Liao, M. Huijben, Z. Zhong, N. Gauquelin, S. Macke, R. J. Green, S. Van Aert, J. Verbeeck, G. Van Tendeloo, K. Held, G. A. Sawatzky, G. Koster, and G. Rijnders, "Controlled lateral anisotropy in correlated manganite heterostructures by interface-engineered oxygen octahedral coupling," Nat. Mater. **15**(4), 425–431 (2016).

[10] D. Kan, R. Aso, R. Sato, M. Haruta, H. Kurata, and Y. Shimakawa, "Tuning magnetic anisotropy by interfacially engineering the oxygen coordination environment in a transition metal oxide," Nat. Mater. **15**(4), 432–437 (2016).
[11] J. M. Rondinelli, S. J. May, and J. W. Freeland, "Control of octahedral connectivity in perovskite oxide heterostructures: An emerging route to multifunctional materials discovery," MRS Bull. **37**(3), 261–270 (2012).
[12] J. Nordlander, M. Campanini, M. D. Rossell, R. Erni, Q. N. Meier, A. Cano, N. A. Spaldin, M. Fiebig, and M. Trassin, "The ultrathin limit of improper ferroelectricity," Nat. Commun. **10**(1), 5591 (2019).
[13] S. Catalano, M. Gibert, V. Bisogni, O. E. Peil, F. He, R. Sutarto, M. Viret, P. Zubko, R. Scherwitzl, A. Georges, G. A. Sawatzky, T. Schmitt, and J.-M. M. Triscone, "Electronic transitions in strained $SmNiO_3$ thin films," APL Mater. **2**(11), 116110 (2014).
[14] S. Catalano, M. Gibert, J. Fowlie, J. Iñiguez, J. M. Triscone, and J. Kreisel, "Rare-earth nickelates RNiO$_3$: Thin films and heterostructures," Rep. Prog. Phys. **81**(4), 046501 (2018).
[15] D. Fuchs, E. Arac, C. Pinta, S. Schuppler, R. Schneider, and H. v. Löhneysen, "Tuning the magnetic properties of $LaCoO_3$ thin films by epitaxial strain," Phys. Rev. B **77**, 014434 (2008).
[16] J. Bak, H. B. Bae, C. Oh, J. Son, and S. Y. Chung, "Effect of lattice strain on the formation of Ruddlesden–Popper faults in heteroepitaxial $LaNiO_3$ for oxygen evolution electrocatalysis," J. Phys. Chem. Lett. **11**(17), 7253–7260 (2020).
[17] B. Mundet, J. Jareño, J. Gazquez, M. Varela, X. Obradors, and T. Puig, "Defect landscape and electrical properties in solution-derived $LaNiO_3$ and $NdNiO_3$ epitaxial thin films," Phys. Rev. Mater. **2**(6), 063607 (2018).
[18] S. G. Jeong, G. Han, S. Song, T. Min, A. Y. Mohamed, S. Park, J. Lee, H. Y. Jeong, Y. Kim, D. Cho, and W. S. Choi, "Propagation control of octahedral tilt in $SrRuO_3$ via artificial heterostructuring," Adv. Sci. **7**, 2001643–2001648 (2020).
[19] T. H. Kim, D. Puggioni, Y. Yuan, L. Xie, H. Zhou, N. Campbell, P. J. Ryan, Y. Choi, J. W. Kim, J. R. Patzner, S. Ryu, J. P. Podkaminer, J. Irwin, Y. Ma, C. J. Fennie, M. S. Rzchowski, X. Q. Pan, V. Gopalan, J. M. Rondinelli, and C. B. Eom, "Polar metals by geometric design," Nature **533**(7601), 68–72 (2016).
[20] S. Catalano, M. Gibert, V. Bisogni, F. He, R. Sutarto, M. Viret, P. Zubko, R. Scherwitzl, G. A. Sawatzky, T. Schmitt, and J. M. Triscone, "Tailoring the electronic transitions of $NdNiO_3$ films through $(111)_{pc}$ oriented interfaces," APL Mater. **3**(6), 062506 (2015).
[21] P. Zubko, S. Gariglio, M. Gabay, P. Ghosez, and J.-M. Triscone, "Interface physics in complex oxide heterostructures," Annu. Rev. Condens. Matter Phys. **2**(1), 141–165 (2011).
[22] A. Ohtomo and H. Y. Hwang, "A high-mobility electron gas at the $LaAlO_3/SrTiO_3$ heterointerface," Nature **427**(6973), 423–426 (2004).
[23] M. Gibert, M. Viret, P. Zubko, N. Jaouen, J. M. Tonnerre, A. Torres-Pardo, S. Catalano, A. Gloter, O. Stéphan, and J. M. Triscone, "Interlayer coupling through a dimensionality-induced magnetic state," Nat. Commun. **7**, 11227 (2016).
[24] M. N. Grisolia, J. Varignon, G. Sanchez-Santolino, A. Arora, S. Valencia, M. Varela, R. Abrudan, E. Weschke, E. Schierle, J. E. Rault, J. P. Rueff, A. Barthélémy, J. Santamaria, and M. Bibes, "Hybridization-controlled charge transfer and induced magnetism at correlated oxide interfaces," Nat. Phys. **12**, 484–492 (2016).
[25] J. Fowlie, C. Lichtensteiger, M. Gibert, H. Meley, P. Willmott, and J. M. Triscone, "Thickness-dependent perovskite octahedral distortions at heterointerfaces," Nano Lett. **19**(6), 4188–4194 (2019).
[26] Z. Liao, R. J. Green, N. Gauquelin, S. Macke, L. Li, J. Gonnissen, R. Sutarto, E. P. Houwman, Z. Zhong, S. Van Aert, J. Verbeeck, G. A. Sawatzky, M. Huijben, G. Koster, G. Rijnders, S. Van Aert, J. Verbeeck, G. A. Sawatzky, M. Huijben, G. Koster, and G. Rijnders, "Long-range domain structure and symmetry engineering by interfacial oxygen octahedral coupling at heterostructure interface," Adv. Funct. Mater. **26**(36), 6627–6634 (2016).
[27] D. L. Proffit, H. W. Jang, S. Lee, C. T. Nelson, X. Q. Pan, M. S. Rzchowski, and C. B. Eom, "Influence of symmetry mismatch on heteroepitaxial growth of perovskite thin films," Appl. Phys. Lett. **93**(11), 111912 (2008).
[28] Z. H. Chen, A. R. Damodaran, R. Xu, S. Lee, and L. W. Martin, "Effect of 'symmetry mismatch' on the domain structure of rhombohedral $BiFeO_3$ thin films," Appl. Phys. Lett. **104**(18), 182908 (2014).
[29] X. Ding, B. Yang, H. Leng, J. H. Jang, J. Zhao, C. Zhang, S. Zhang, G. Cao, J. Zhang, R. Mishra, J. Yi, D. Qi, Z. Gai, X. Zu, S. Li, B. Huang, A. Borisevich, and L. Qiao, "Crystal symmetry engineering in epitaxial perovskite superlattices," Adv. Funct. Mater. **31**(47), 2106466 (2021).
[30] L. Qiao, J. H. Jang, D. J. Singh, Z. Gai, H. Xiao, A. Mehta, R. K. Vasudevan, A. Tselev, Z. Feng, H. Zhou, S. Li, W. Prellier, X. Zu, Z. Liu, A. Borisevich, A. P. Baddorf, and M. D. Biegalski, "Dimensionality controlled octahedral symmetry-mismatch and functionalities in epitaxial $LaCoO_3/SrTiO_3$ heterostructures," Nano Lett. **15**(7), 4677–4684 (2015).
[31] M. D. Biegalski, L. Qiao, Y. Gu, A. Mehta, Q. He, Y. Takamura, A. Borisevich, and L. Q. Chen, "Impact of symmetry on the ferroelectric properties of $CaTiO_3$ thin films," Appl. Phys. Lett. **106**(16), 162904 (2015).
[32] A. Vailionis, H. Boschker, W. Siemons, E. P. Houwman, D. H. A. Blank, G. Rijnders, and G. Koster, "Misfit strain accommodation in epitaxial ABO_3 perovskites: Lattice rotations and lattice modulations," Phys. Rev. B **83**(6), 064101 (2011).
[33] R. Gao, Y. Dong, H. Xu, H. Zhou, Y. Yuan, V. Gopalan, C. Gao, D. D. Fong, Z. Chen, Z. Luo, and L. W. Martin, "Interfacial octahedral rotation mismatch control of the symmetry and properties of $SrRuO_3$," ACS Appl. Mater. Interfaces **8**(23), 14871–14878 (2016).
[34] T. C. van Thiel, J. Fowlie, C. Autieri, N. Manca, M. Šiškins, D. Afanasiev, S. Gariglio, and A. D. Caviglia, "Coupling lattice instabilities across the interface in ultrathin oxide heterostructures," ACS Mater. Lett. **2**(4), 389–394 (2020).
[35] Y. E. Suyolcu, K. Fürsich, M. Hepting, Z. Zhong, Y. Lu, Y. Wang, G. Christiani, G. Logvenov, P. Hansmann, M. Minola, B. Keimer, P. A. Van Aken, and E. Benckiser, "Control of the metal-insulator transition in $NdNiO_3$ thin films through the interplay between structural and electronic properties," Phys. Rev. Mater. **5**, 045001 (2021).
[36] W. Wang, L. Li, J. Liu, B. Chen, Y. Ji, J. Wang, G. Cheng, Y. Lu, G. Rijnders, G. Koster, W. Wu, and Z. Liao, "Magnetic domain engineering in $SrRuO_3$ thin films," Npj Quantum Mater. **5**, 73 (2020).
[37] A. T. Mulder, N. A. Benedek, J. M. Rondinelli, and C. J. Fennie, "Turning ABO_3 antiferroelectrics into ferroelectrics: Design rules for practical rotation-driven ferroelectricity in double perovskites and $A_3B_2O_7$ Ruddlesden-popper compounds," Adv. Funct. Mater. **23**(38), 4810–4820 (2013).
[38] E. Bousquet, M. Dawber, N. Stucki, C. Lichtensteiger, P. Hermet, S. Gariglio, J. M. Triscone, and P. Ghosez, "Improper ferroelectricity in perovskite oxide artificial superlattices," Nature **452**, 732–736 (2008).
[39] J. M. Rondinelli and C. J. Fennie, "Octahedral rotation-induced ferroelectricity in cation ordered perovskites," Adv. Mater. **24**(15), 1961–1968 (2012).
[40] S. Ghosh, H. Das, and C. J. Fennie, "Linear magnetoelectricity at room temperature in perovskite superlattices by design," Phys. Rev. B **92**(18), 184112 (2015).
[41] M. Brahlek, A. K. Choquette, C. R. Smith, R. Engel-Herbert, and S. J. May, "Structural refinement of *Pbnm*-type perovskite films from analysis of half-order diffraction peaks," J. Appl. Phys. **121**(4), 045303 (2017).
[42] A. K. Choquette, C. R. Smith, R. J. Sichel-Tissot, E. J. Moon, M. D. Scafetta, E. Di Gennaro, F. Miletto Granozio, E. Karapetrova, and S. J. May, "Octahedral rotation patterns in strained $EuFeO_3$ and other *Pbnm* perovskite films: Implications for hybrid improper ferroelectricity," Phys. Rev. B **94**, 024105 (2016).
[43] D. Kan, R. Aso, H. Kurata, and Y. Shimakawa, "Thickness-dependent structure–property relationships in strained (110) $SrRuO_3$ Thin Films," Adv. Funct. Mater. **23**(9), 1129–1136 (2013).
[44] M. J. Hÿtch, E. Snoeck, and R. Kilaas, "Quantitative measurement of displacement and strain fields from HREM micrographs," Ultramicroscopy **74**(3), 131–146 (1998).
[45] Y. Zhu, C. Ophus, J. Ciston, and H. Wang, "Interface lattice displacement measurement to 1 pm by geometric phase analysis on aberration-corrected HAADF STEM images," Acta Mater. **61**(15), 5646–5663 (2013).
[46] D. Cooper, T. Denneulin, N. Bernier, A. Béché, and J. L. Rouvière, "Strain mapping of semiconductor specimens with nm-scale resolution in a transmission electron microscope," Micron **80**, 145–165 (2016).
[47] G. Catalan, A. Lubk, A. H. G. Vlooswijk, E. Snoeck, C. Magen, A. Janssens, G. Rispens, G. Rijnders, D. H. A. Blank, and B. Noheda, "Flexoelectric rotation of polarization in ferroelectric thin films," Nat. Mater. **10**(12), 963–967 (2011).
[48] Y. L. Tang, Y. L. Zhu, X. L. Ma, A. Y. Borisevich, A. N. Morozovska, E. A. Eliseev, W. Y. Wang, Y. J. Wang, Y. B. Xu, Z. D. Zhang, and S. J. Pennycook,

"Observation of a periodic array of flux-closure quadrants in strained ferroelectric $PbTiO_3$ films," Science **348**(6234), 547–551 (2015).
[49]G. Catalan, "Progress in perovskite nickelate research," Phase Transitions **81**(7–8), 729–749 (2008).
[50]S. Middey, J. Chakhalian, P. Mahadevan, J. W. W. Freeland, A. J. J. Millis, and D. D. D. Sarma, "Physics of ultrathin films and heterostructures of rare-earth nickelates," Annu. Rev. Mater. Res. **46**(1), 305–314 (2016).
[51]S. Amisi, E. Bousquet, K. Katcho, and P. Ghosez, "First-principles study of structural and vibrational properties of $SrZrO_3$," Phys. Rev. B **85**, 064112 (2012).
[52]N. Miao, N. C. Bristowe, B. Xu, M. J. Verstraete, and P. Ghosez, "First-principles study of the lattice dynamical properties of strontium ruthenate," J. Phys.: Condens.Matter **26**(3), 035401 (2014).
[53]A. K. Choquette, R. Colby, E. J. Moon, C. M. Schlepütz, M. D. Scafetta, D. J. Keavney, and S. J. May, "Synthesis, structure, and spectroscopy of epitaxial $EuFeO_3$ thin films," Cryst. Growth Des. **15**(3), 1105–1111 (2015).
[54]J. Y. Zhang, J. Hwang, S. Raghavan, and S. Stemmer, "Symmetry lowering in extreme-electron-density perovskite quantum wells," Phys. Rev. Lett. **110**, 256401 (2013).
[55]C. Ghica, R. F. Negrea, L. C. Nistor, C. F. Chirila, and L. Pintilie, "Nanoscale monoclinic domains in epitaxial $SrRuO_3$ thin films deposited by pulsed laser deposition," J. Appl. Phys. **116**(2), 023516 (2014).
[56]B. H. Goodge, I. El Baggari, S. S. Hong, Z. Wang, D. G. Schlom, H. Y. Hwang, and L. F. Kourkoutis, "Disentangling coexisting structural order through phase lock-in analysis of atomic-resolution STEM data," Microsc. Microanal. **28**(2), 404–411 (2022).
[57]C. Domínguez, A. B. Georgescu, B. Mundet, Y. Zhang, J. Fowlie, A. Mercy, A. Waelchli, S. Catalano, D. T. L. Alexander, P. Ghosez, A. Georges, A. J. Millis, M. Gibert, and J. M. Triscone, "Length scales of interfacial coupling between metal and insulator phases in oxides," Nat. Mater. **19**, 1182–1187 (2020).
[58]D. T. L. Alexander, H. Meley, M. M. Schmitt, B. Mundet, P. Ghosez, J.-M. Triscone, and S. Gariglio, "Switching plane: A novel crystalline interface in orthorhombic perovskite films," arXiv:2401.08798 (2024).
[59]H. Meley, K. Deep, L. Oberson, J. De Bruijckere, D. T. L. Alexander, J. M. Triscone, P. Ghosez, and S. Gariglio, "Structural analysis of $LaVO_3$ thin films under epitaxial strain," APL Mater. **6**(4), 046102 (2018).
[60]J. Fowlie, B. Mundet, C. Toulouse, A. Schober, M. Guennou, C. Domínguez, M. Gibert, D. T. L. Alexander, J. Kreisel, and J. M. Triscone, "Crossover between distinct symmetries in solid solutions of rare earth nickelates," APL Mater. **9**(8), 081119 (2021).
[61]Q. Zheng, N. J. Schreiber, H. Zheng, J. Yan, M. A. McGuire, J. F. Mitchell, M. Chi, and B. C. Sales, "Real space visualization of competing phases in $La_{0.6}Sr_{2.4}Mn_2O_7$ single crystals," Chem. Mater. **30**(21), 7962–7969 (2018).
[62]E. Detemple, Q. M. Ramasse, W. Sigle, G. Cristiani, H. U. Habermeier, B. Keimer, and P. A. Van Aken, "Ruddlesden-Popper faults in $LaNiO_3/LaAlO_3$ superlattices," J. Appl. Phys. **112**(1), 013509 (2012).
[63]M. Medarde, J. García-Muñoz, S. Rosenkranz, X. Granados, J. Fontcuberta, and P. Lacorre, "Crystallographic and magnetic study of $Nd_{0.7}La_{0.3}NiO_3$," Physica B **194-196**(1), 367–368 (1994).
[64]J. Bak, H. B. Bae, J. Kim, J. Oh, and S. Y. Chung, "Formation of two-dimensional homologous faults and oxygen electrocatalytic activities in a perovskite nickelate," Nano Lett. **17**(5), 3126–3132 (2017).
[65]K. Lee, B. Y. Wang, M. Osada, B. H. Goodge, T. C. Wang, Y. Lee, S. Harvey, W. J. Kim, Y. Yu, C. Murthy, S. Raghu, L. F. Kourkoutis, and H. Y. Hwang, "Linear-in-temperature resistivity for optimally superconducting $(Nd,Sr)NiO_2$," Nature **619**(7969), 288–292 (2023).
[66]R. J. Jiang, Y. Cao, W. R. Geng, M. X. Zhu, Y. L. Tang, Y. L. Zhu, Y. Wang, F. Gong, S. Z. Liu, Y. T. Chen, J. Liu, N. Liu, J. H. Wang, X. D. Lv, S. J. Chen, and X. L. Ma, "Atomic insight into the successive antiferroelectric-ferroelectric phase transition in antiferroelectric oxides," Nano Lett. **23**(4), 1522–1529 (2023).
[67]W. R. Geng, X. W. Guo, Y. L. Zhu, Y. J. Wang, Y. L. Tang, M. J. Han, Y. P. Feng, M. J. Zou, B. Wu, J. Y. Ma, W. T. Hu, and X. L. Ma, "Oxygen octahedral coupling mediated ferroelectric-antiferroelectric phase transition based on domain wall engineering," Acta Mater. **198**, 145–152 (2020).
[68]A. Raji, Z. Dong, V. Porée, A. Subedi, X. Li, B. Mundet, L. Varbaro, C. Domínguez, M. Hadjimichael, B. Feng, A. Nicolaou, J.-P. Rueff, D. Li, and A. Gloter, "Valence-ordered thin-film nickelate with tri-component nickel coordination prepared by topochemical reduction," ACS Nano **18**, 4077 (2024).
[69]M. Hadjimichael, A. Waelchli, B. Mundet, S. McKeown Walker, G. De Luca, J. Herrero-Martín, M. Gibert, S. Gariglio, and J. M. Triscone, "Structural and electronic properties of $SrCuO_{2+\delta}$ thin films," APL Mater. **10**(10), 101112 (2022).